JCI insight

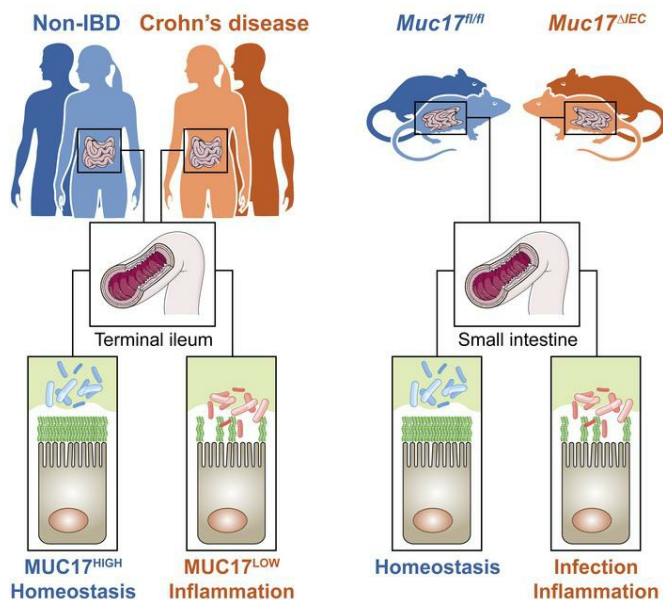# MUC17 is an essential small intestinal glycocalyx component that is disrupted in Crohn's disease

Elena Layunta, … , Bruce A. Vallance, Thaher Pelaseyed

Research In-Press Preview Cell biology Gastroenterology

Graphical abstract

MUC17 is an essential small intestinal glycocalyx component that is disrupted in Crohn's disease

Elena Layunta[1], Sofia Jäverfelt[1], Fleur C. van de Koolwijk[1], Molly Sivertsson[1], Brendan Dolan[1], Liisa Arike[1], Sara Thulin[1], Bruce A. Vallance[2], and Thaher Pelaseyed[1]*

1. Department of Medical Biochemistry and Cell Biology, Institute of Biomedicine, University of Gothenburg, Gothenburg, Sweden.

2. Division of Gastroenterology, Hepatology and Nutrition, Department of Pediatrics, BC Children's Hospital Research Institute, University of British Columbia, Vancouver, Canada.

*Corresponding author.

Thaher Pelaseyed

Department of Medical Biochemistry and Cell Biology

Institute of Biomedicine

University of Gothenburg,

Box 440

405 30 Gothenburg,

Sweden

Telephone number +46 (0) 31 786 31 54

Email thaher.pelaseyed@medkem.gu.se

Authorship was assigned based on ICMJE criteria

Conflict-of-interest statement: The authors have declared that no conflict of interest exists.

Abstract

Crohn's disease (CD) is the chronic inflammation of the terminal ileum and colon triggered by a dysregulated immune response to bacteria, but insights into specific molecular perturbations at the critical bacteria-epithelium interface are limited. Here we report that the membrane mucin MUC17 protected small intestinal enterocytes against commensal and pathogenic bacteria. In non-inflamed CD ileum, reduced MUC17 levels and a compromised glycocalyx barrier allowed recurrent bacterial contact with enterocytes. *Muc17* deletion in mice rendered the small intestine particularly prone to atypical bacterial infection while maintaining resistance to colitis. The loss of Muc17 resulted in spontaneous deterioration of epithelial homeostasis and in the extra-intestinal translocation of bacteria. Finally, Muc17-deficient mice harbored specific small intestinal bacterial taxa observed in CD patients. Our findings highlight MUC17 as an essential regiospecific line of defense in the small intestine with relevance for early epithelial defects in CD.

Introduction

Mucins are critical for the gastrointestinal defense system (1, 2). In the mouse distal colon, the gel-forming Muc2 forms an attached impenetrable mucus layer that separates bacteria from the epithelium (3). Defects in core mucus components constitute early steps in the pathogenesis of ulcerative colitis, a form of inflammatory bowel disease (IBD) in humans (4). In contrast, the mucus of the small intestine is non-attached and permeable to luminal material including bacteria (5). This regiospecific difference demands a distinct defense mechanism to manage host-microbiota interactions. In this context, the role of membrane mucins in small intestinal enterocytes is unexplored, due to limited insight into their gene sequences (6) and difficulties preserving them in fixed tissues. MUC17, alongside MUC13, is a conserved heavily *O*-glycosylated membrane mucin positioned at the apical brush border of differentiated enterocytes (7, 8) (Figure 1A). In the mouse small intestine, the homeostatic cytokine IL-22 induces Muc17 expression and the establishment of a surface glycocalyx that in *ex vivo* experiments prevents direct attachment of bacteria to the brush border (9). Crohn's disease (CD) is an IBD subtype characterized by patchy chronic inflammation involving dysregulated immune responses to the gut bacteria (10). Unlike UC that is limited to the colon, CD affects both the small and large intestines, with a third of patients displaying inflammation exclusively in the terminal ileum (11). Susceptibility to ileal CD has been linked to mutations in the intracellular peptidoglycan sensor *NOD2* and autophagy protein *ATG16L1*, which impair the detection and degradation of invasive bacteria that cross the apical cell membrane (12-14). However, apart from reports of transcriptional changes in enterocyte brush border components (15), it is still unclear whether CD patients have any functional defects at the apical membrane, upstream of the intracellular innate immune response to bacteria. MUC17 is both transcriptionally and structurally associated with the

brush border (9), but the role of MUC17 in epithelial defense and whether MUC17 expression and glycocalyx integrity are compromised in CD are not known.

Here, we analyzed non-inflamed ileal biopsies from CD patients and non-IBD controls together with a genetic mouse model to define the function of MUC17 in the intestine. CD patients displayed decreased MUC17 levels and a glycocalyx that was more permeable to bacteria. In mice, intestine-specific deletion of the *Muc17* gene was dispensable for colonic inflammation whilst rendering the small intestine abnormally sensitive to infection by the attaching effacing bacterium *Citrobacter rodentium* (*C. rodentium*). *Muc17*$^{\Delta IEC}$ mice also suffered spontaneous deterioration of the epithelial cell barrier and displayed translocation of viable bacteria to extra-intestinal tissues. Lastly, we showed that Muc17 regulates the abundance of specific bacterial taxa in the small intestine, including bacteria enriched in CD patients. Thus, the *Muc17*$^{\Delta IEC}$ model reproduces fundamental manifestations of CD, suggesting that MUC17 is essential for protecting the small intestine against commensal and pathogenic bacteria.

Results

Decreased MUC17 levels and glycocalyx integrity in ileal Crohn's disease

In humans, MUC17 is exclusively expressed in differentiated enterocytes of the small intestine (Figure 1, B-C). We analyzed the expression of MUC17 in histological sections from the non-inflamed terminal ileum of CD patients and a control group with non-IBD-related pathologies (Supplemental Table 1). MUC17 levels were significantly reduced in the enterocyte brush border of the CD compared to non-IBD ileum, which showed a typical MUC17 staining in the brush border marked by Ezrin (Figure 1D). Membrane mucin MUC13 was not altered between the two cohorts (Figure 1E). Next, we analyzed ileal biopsies with an *ex vivo* time-lapse glycocalyx permeability assay (9), which measures the ability of the glycocalyx to separate GFP-expressing *Escherichia coli* (*E. coli*$^{GFP+}$) from the brush border (see materials and methods). In line with decreased apical MUC17 in CD ileum, the frequency of *E. coli*$^{GFP+}$ that approached the brush border was significantly higher in CD compared to non-IBD controls, indicating reduced glycocalyx barrier integrity in CD patients (Figure 1F, Supplemental Figure 1A, Movie 1). Subsequent staining of biopsies analyzed by glycocalyx permeability assay for MUC17 surface staining showed that non-IBD samples had a significantly higher relative MUC17 surface expression than CD samples (1.26 ± 0.51 versus 0.33 ± 0.07) (Supplemental Figure 1, B-C). Thus, the non-inflamed CD ileum exhibits an impaired glycocalyx barrier and reduced MUC17 levels in the apical brush border.

The *Muc17*$^{\Delta IEC}$ mouse lacks a small intestinal glycocalyx

The loss of glycocalyx integrity in CD ileum suggests that the loss of apical MUC17 is an early defect resulting in increased bacterial contact with the brush border. To test this hypothesis, we generated a conditional *Muc17*$^{\Delta IEC}$ mouse by crossing *Muc17*$^{fl/fl}$ and *Vil1-Cre* mice expressing the Cre recombinase in intestinal epithelial cells (Supplemental Figure 2, A-

C). Unlike human MUC17, murine Muc17 is expressed in both the small intestine and colon (Figure 1A, Figure 2, A-B, Supplemental Figure 3, Supplemental Figure 4). The successful deletion of *Muc17* was thus confirmed in the duodenum, jejunum (Si5), ileum (Si8), proximal colon (PC), and distal colon (DC) (Figure 1A, Figure 2C, Supplemental Figure 3, Supplemental Figure 4). High-resolution microscopy of small intestinal enterocytes revealed that MUC17 was lacking from the tips of microvilli in *Muc17*$^{\Delta IEC}$ mice. (Figure 2D). *Muc17* deletion was also demonstrated in microvillus-derived luminal vesicles isolated from the small intestinal (16, 17) (Supplemental Figure 2D). To evaluate the impact of *Muc17* deletion on other mucins, we performed proteomic analysis of isolated small intestinal epithelial cells from *Muc17*$^{fl/fl}$ and *Muc17*$^{\Delta IEC}$ cohoused littermates. Deletion of *Muc17* did not result in a compensatory change in the abundance of Muc13 or the gel-forming Muc2 (Figure 2E, Supplemental Table 2). Moreover, *Muc17*$^{\Delta IEC}$ mice did not exhibit alterations in tissue morphology of the small intestine or distal colon (Supplemental Figure 2E). Notably, the deletion of *Muc17* had no impact on brush border morphology or cellular polarity, evaluated by the brush border markers Ezrin and Cdhr5, and basolateral EpCAM (Supplemental Figure 2, F-G). Mucin *O*-glycans convert the glycocalyx into a size-selective diffusion barrier and shield against bacterial degradation (1, 9). To determine if the loss of Muc17 impacted the density of glycocalyx *O*-glycans, we employed *in vivo* bioorthogonal labeling using GalNAz, the azide derivative of N-Acetylgalactosamine (GalNAc), the first glycan added to serines or threonines during mucin-type *O*-glycosylation (18). GalNAz intensity was significantly reduced in the small intestinal brush border of *Muc17*$^{\Delta IEC}$ mice compared to controls but remained unchanged in the colonic brush border (Figure 2F). The *O*-glycan deficit of the small intestinal glycocalyx was further supported by decreased staining with Aleuria aurantia lectin (AAL) and wheat germ agglutinin (WGA), which bind fucose and *N*-acetylglucosamine (Supplemental Figure 2H). Differential expression analysis did not detect

any significant changes in glycosyltransferases involved in initiation, branching or capping of mucin-type *O*-glycans (Supplemental Figure 2I, Supplemental Table 2), indicating that reduced GalNAz incorporation in the brush border of *Muc17^ΔIEC^* mice was a result of the absence of Muc17 and not an altered glycosylation machinery. Thus, under baseline conditions *Muc17* deletion results in an explicit loss of the mucin-based glycocalyx without impacting the overall tissue and cell morphology of the small intestine.

Deletion of *Muc17* causes abnormal small intestinal susceptibility to *Citrobacter Rodentium* infection

Since we did not observe any baseline phenotype in *Muc17^ΔIEC^* mice, cohoused *Muc17^fl/fl^* and *Muc17^ΔIEC^* littermates were infected with *C. rodentium*, a natural murine pathogen that normally causes a self-limiting infection in the distal colon (19). Infection kinetics in each group were monitored over a period of 21 days post-infection (dpi) (Figure 3A). Regardless of genotype, fecal *C. rodentium* counts peaked at 7-9 dpi and declined below the limit of detection (LOD) by 17 dpi (Figure 3B). Both groups exhibited a slight but comparable weight loss during the initial infection phase (1-3 dpi) (Figure 3C). Next, we quantified *C. rodentium* colonization in the luminal and mucosal compartments of the jejunum (Si5), ileum (Si8) and distal colon (DC) at 3 days post-infection. As expected, *Muc17^fl/fl^* mice exhibited a robust colonization in DC (Figure 3, D-E). In *Muc17^ΔIEC^* Si5, however, we observed three orders of magnitude higher *C. rodentium* counts compared to the control group (Figure 3, D-E). The abnormal *C. rodentium* infection of Si5 was not limited to the luminal compartment but was also detected in the mucosa, indicating that the small intestinal epithelium was more susceptible to *C. rodentium* infection in the absence of Muc17 and a glycocalyx. Greater pathogen counts were also observed in the mucosa of *Muc17^ΔIEC^* DC compared to the infected controls (Figure 3E). There was also a trend towards increased translocation of *C.*

rodentium to the peripheral tissues in *Muc17$^{\Delta IEC}$* mice at 7 dpi (Figure 3F). Notably, across all tissues and time points post-infection, a larger fraction of *Muc17$^{\Delta IEC}$* mice carried a detectible pathogen burden compared to *Muc17$^{fl/fl}$* mice (Supplemental Figure 5). At 7 days post-infection, 91±6 % of all *Muc17$^{\Delta IEC}$* mice exhibited a small intestinal infection compared to only 54±13 % of the *Muc17$^{fl/fl}$* mice. A similar analysis of colonic pathogen burden did not reveal any significant difference between the groups. Accordingly, the relative risk of *C. rodentium* infection in *Muc17$^{\Delta IEC}$* mice peaked in Si5 mucosa and decreased towards the DC, suggesting that Muc17 primarily serves as a small intestinal defense mechanism during bacterial infection (Figure 3G). *Muc17* deletion also resulted in a higher relative risk of pathogen translocation to the peripheral tissues (Figure 3H). Histological analysis 3 days post-infection revealed numerous *C. rodentium^{GFP+}* cells in contact with the epithelium at villus apexes, intervillar regions, and the crypt compartment of *Muc17$^{\Delta IEC}$* Si5, whereas *C. rodentium^{GFP+}* was not detected in *Muc17$^{fl/fl}$* (Figure 3I). Assessment of the distal colon showed *C. rodentium^{GFP+}* at the surface epithelium and in the crypts of *Muc17$^{\Delta IEC}$* mice (Figure 3, J-K). Collectively, the absence of Muc17 caused an abnormal small intestinal susceptibility to *C. rodentium*, indicating that Muc17 is essential for protecting the small intestinal epithelium against pathogenic bacteria.

Muc17$^{\Delta IEC}$ mice display spontaneous loss of epithelial homeostasis

Given that Muc17 protected the small intestine against pathogenic infection, we reasoned that *Muc17* deletion might also allow commensal bacteria to make direct contact with enterocytes and thereby disrupt epithelial homeostasis. Thus, we turned our attention to unchallenged 6-8-week-old cohoused *Muc17$^{fl/fl}$* and *Muc17$^{\Delta IEC}$* littermates maintained under standard pathogen-free (SPF) conditions. Histological analysis of Si5 did not reveal any genotype-dependent differences in crypt number, villus length, or goblet cell frequency (Figure 4A,

Supplemental Figure 2E). Next, Si5 explants were flushed, and fixed to preserve the mucosal compartment, and the distribution of bacteria in relation to the brush border was assessed using confocal microscopy and automatic image segmentation. Compared to $Muc17^{fl/fl}$, significantly higher numbers of bacteria were directly bound to the brush border of $Muc17^{\Delta IEC}$ mice (Figure 4B). Findings were supported by fluorescence *in situ* hybridization (FISH) with a universal eubacterial probe, showing bacteria in direct contact with the $Muc17^{\Delta IEC}$ brush border (Figure 4C). Uncontrolled bacterial interactions with the epithelium can trigger increased epithelial proliferation and cell death (20, 21). Correspondingly, we observed a significant expansion of proliferative mKi67^{+} epithelial cells within the crypt compartment of $Muc17^{\Delta IEC}$ Si5 (Figure 4D). Free nuclear DNA 3′-OH termini generated by single-strand breaks are hallmarks of apoptosis. Compared to controls, $Muc17^{\Delta IEC}$ Si5 displayed a higher number of TUNEL-positive apoptotic cells at villus apexes (Figure 4E). Next, we used mass spectrometry to evaluate the impact of $Muc17$ deletion on epithelial cell homeostasis. Label-free protein quantification in epithelial cells from 5-, 8- and 36-weeks-old $Muc17^{fl/fl}$ and $Muc17^{\Delta IEC}$ mice revealed altered protein abundance in 0.25-1.00% of the proteome, mainly affecting brush border-associated proteins (Figure 4F, Supplemental Table 2). Specifically, we observed a higher abundance of Rho guanine nucleotide exchange factor 26 (Arhgef26) in epithelial cells of 8-week-old $Muc17^{\Delta IEC}$ mice . Arhgef26 participates in enterocyte membrane remodeling and ruffling during bacterial invasion (22) (Figure 4F, Supplemental Figure 6). We also detected higher abundance of the antimicrobial proteins Lyz1 and Reg3b in 36-week-old $Muc17^{\Delta IEC}$ mice (Figure 4F, Supplemental Figure 6), reflecting a host response to persistent bacterial challenges exerted on the intestinal epithelium in $Muc17^{\Delta IEC}$ mice. Further assessment showed no histological signs of inflammation (Supplemental Figure 7) but a significant upregulation of the proinflammatory cytokine *Il-6* in the small intestine of $Muc17^{\Delta IEC}$ mice compared to wild-type littermates

(Figure 4G). Collectively, our results suggest that a higher burden of bacteria at the epithelial surface results in the spontaneous loss of epithelial homeostasis and inflammation.

Muc17 is dispensable for protection against chemically induced colitis

To define the protective role of Muc17 in the murine distal colon, cohoused $Muc17^{fl/fl}$ and $Muc17^{\Delta IEC}$ littermates were subjected to 7-day *ad libitum* administration of dextran sodium sulfate (DSS), a chemically induced model of human ulcerative colitis (Supplemental Figure 8A). $Muc17^{\Delta IEC}$ mice displayed a reduction in weight compared to wild-type mice, but only at the end of the intervention (day 6). (Supplemental Figure 8B). While there was a significant shortening of the colon in $Muc17^{\Delta IEC}$ mice after 7 days (Supplemental Figure 8C), only a moderately increased susceptibility to DSS was measured by stool consistency, fecal blood score, overall disease activity index, and survival (Supplemental Figure 8, D-G). Our observations were supported by histological analysis of Si5 and DC, which corroborated that $Muc17^{fl/fl}$ and $Muc17^{\Delta IEC}$ mice responded similarly to DSS-induced colitis (Supplemental Figure 8, H-I). The late onset of moderate inflammation in the absence of Muc17 contrasted acute induction of severe colitis in $C3GnT^{-/-}$, $Vamp8^{-/-}$, and $Tgm3^{-/-}$ mice with defects in Muc2 glycosylation, secretion, and crosslinking (23-25). Thus, we concluded that Muc17 does not play a critical protective role in the distal colon.

Further assessment of $Muc17^{\Delta IEC}$ mice under baseline conditions did not show any deviations in the number of crypts, crypt length, or goblet cell frequency in the distal colon (Supplemental Figure 9A, Supplemental Figure 2E). Next, we quantified the barrier properties of the inner mucus layer (IML) separating bacteria from the epithelium (26). FISH showed a defined separation of bacteria from the epithelium in 6-8-week-old $Muc17^{fl/fl}$ and $Muc17^{\Delta IEC}$ mice (Supplemental Figure 9B*). Ex vivo* mucus penetrability analysis in viable explants from 6–8- or 36-40 week-old mice, evaluating the penetration of microbeads

through the IML, showed that both *Muc17*$^{\Delta IEC}$ and *Muc17*$^{fl/fl}$ mice maintain an impenetrable IML typically observed in wild-type mice (3) (Figure S, 8C-D). *Muc17*$^{\Delta IEC}$ mice did however display elevated occurrence of shed cells (Supplemental Figure 9D) and increased epithelial cell proliferation measured by mKi67$^+$ (Supplemental Figure 9E). The fact that *Muc17*$^{\Delta IEC}$ mice were susceptible to small intestinal infection by a colonic pathogen strongly suggests that Muc17 is a critical, but likely not the only, defense mechanism that protects the small intestine against pathogens. That *Muc17*$^{\Delta IEC}$ mice are only slightly more susceptible to acute DSS challenge, a model for colonic inflammation (colitis), suggests that Muc17 does not play a critical role in the colonic defense system. This is logical because the impenetrable inner mucus layer, which constitutes the main defense barrier of the colon, remains intact in the absence of Muc17 (Supplemental Figure 9, C-D). Together, our findings confirm that Muc17 is not required for the protection of the distal colon against commensal bacteria.

Muc17 deletion alters the small intestinal microbiota and elicits extra-intestinal translocation of bacteria

Muc17 deletion resulted in susceptibility to *C. rodentium* and increased contact between commensal bacteria and small intestinal enterocytes, but the precise effect of Muc17 on the regiospecific composition of the microbiota is not understood. We thus analyzed bacterial genomic DNA from the luminal compartment of the small intestine and colon of cohoused *Muc17*$^{fl/fl}$ and *Muc17*$^{\Delta IEC}$ littermates by 16S rRNA gene sequencing. While there was no significant difference in species richness and evenness (alpha diversity) between the two groups (Figure 5, A and D), the beta diversity based on Bray-Curtis distances revealed distinct patterns in the microbiota of *Muc17*$^{fl/fl}$ and *Muc17*$^{\Delta IEC}$ mice (Figure 5, B and E). The small intestinal community of *Muc17*$^{\Delta IEC}$ mice was characterized by a higher abundance of the classes of *Actinobacteria*, *Bacteroidia*, *Coriobacteria*, and *gammaproteobacteria* (Figure

5C), while the colonic microbiota shifted towards *Clostridia*, *Coriobacteria*, and *Desulfovibrionia* (Figure 5F). Linear discriminant analysis effect size (LEfSe) analysis showed a depletion of *Firmicutes*, *Bacilli* and the genus *Dubosiella* belonging to the *Erysipelotrichales* from the *Muc17*$^{\Delta IEC}$ small intestine (Figure 5G, Supplemental Figure 10A). The small intestinal alterations in composition were largely reproduced in the *Muc17*$^{fl/fl}$ colon, with the enrichment of *Erysipelotrichales* and *Dubosiella* alongside *Lactobacillus* (Figure 5G, Supplemental Figure 10B). In addition, *Coriobacteriales*, *Lachnoclostridium*, and *Marvinbryantia* were enriched in the *Muc17*$^{\Delta IEC}$ colon (Figure 5G, Supplemental Figure 10B). Combined, the affected genera comprised an average of 15%-20% of the detected operational taxonomic units. Since the microbiota composition varies along the intestine (27), we assessed the regional distribution of the differentially enriched bacterial taxa. *Bacilli*, *Coriobacteriia*, and *Erysipelotrichales,* had a primarily small intestinal niche, with *Erysipelotrichales* dominating the jejunum (Si5) (Figure 5G), thus suggesting a transmission of compositional changes from the small intestine to colon. Collectively, *Muc17* deletion induced a substantial shift in the abundance of specific bacteria that colonize the small intestine (Supplemental Figure 10C), suggesting that Muc17 regulates the regiospecific selection of commensal bacteria.

In ileal Crohn's disease, displacement of mucosa-associated bacteria from the site of inflammation to mesenteric adipose tissue induces the expansion of encapsulating "creeping fat" (28). Bacterially induced enlargement of visceral adipose tissue also occurs in mice that fail to control microbial translocation (29). Under baseline SPF conditions, *Muc17*$^{\Delta IEC}$ mice displayed a higher total body mass (Figure 5H) and larger abdominal fat pads compared to age-matched *Muc17*$^{fl/fl}$ cohoused littermates (Figure 5I). Subsequently, we asked if *Muc17*$^{\Delta IEC}$ mice displayed translocation of commensal bacteria to extra-intestinal tissues. Absolute 16S rRNA gene quantification uncovered significantly higher counts in the MLNs and spleen of

Muc17$^{\Delta IEC}$ mice compared to wild-types (Figure 5J). Bacterial quantification was complemented with anaerobic culturing of viable bacteria from the affected tissues. Heavy bacterial growth was observed in 92% of *Muc17*$^{\Delta IEC}$ MLNs, with the remaining 8% exhibiting light growth (Figure 5, K-L). In *Muc17*$^{fl/fl}$ mice, 33% of MLNs were clear of bacteria and 67% exhibited only light growth. We also observed a higher number of *Muc17*$^{\Delta IEC}$ spleens with heavy bacterial growth compared to control tissues (Figure 5K). Sequencing of the 16S gene identified the translocated bacteria as *Escherichia coli*, *Staphylococcus* spp., and *Ligilactobacillus murinus* (Figure 5M), the latter described as a translocating strain (30). Thus, we concluded that viable commensal bacteria penetrate the intestinal epithelial cell barrier in the absence of Muc17, highlighting its key role in small intestinal barrier function.

Discussion

It is increasingly understood that the defensive properties of gel-forming mucins are important in protection against the development of human IBD (4), but the role of membrane mucins still remains elusive. In this study, we used a conditional mouse model to identify Muc17 as essential for the regiospecific protection of the small intestine against commensal and pathogenic bacteria. Noticeably, a reduction in MUC17 levels in the enterocyte brush border and an impaired glycocalyx protection against bacteria was observed already in the non-inflamed ileum of CD patients. Our findings suggests that membrane mucin and glycocalyx dysfunction precedes inflammation in CD.

The mechanisms underlying CD include genetic factors, such as *NOD2* mutations that impair the sensing and removal of intracellular bacteria (10). These defects in turn trigger immune responses that evoke chronic inflammation. While there are no known disease-associated mutations in the *MUC17* gene and *MUC17* mRNA levels remain unaltered in the non-inflamed ileum of CD patients (31), studies have reported an altered glycocalyx ultrastructure in ileal CD (15). However, the implications of compromised MUC17 protein and glycocalyx barrier function in CD have not been addressed. In this study, we identified decreased MUC17 levels and a weakened glycocalyx in ileal CD to allow for increased bacteria-epithelium interactions. The results find mechanistic support in our earlier studies of murine small intestinal explants demonstrating that Muc17 forms the enterocyte glycocalyx (9). We also showed that the formation of the glycocalyx by Muc17 is induced by IL-22, a critical regulator of antibacterial defenses, including antimicrobial peptides (Reg3b and Reg3g) and mucin fucosylation via *FUT2* (32). Notably, many IBD risk genes, such as *IL23R*, *JAK1/2*, *TYK2*, and *STAT3*, participate in IL-22 signaling (32) and the frequency of IL-22-producing type 3 innate lymphoid cells is lower in CD patients (33).

Investigations on the functional role of gastrointestinal membrane mucins *in vivo* remain sparse. MUC1/Muc1 is normally expressed in the human and murine stomach and studies in *Muc1*$^{-/-}$ mice have shown a protective role in gastric *Helicobacter pylori* infection (34). MUC13 has been suggested to act as decoy for the SiiE adhesin of *Salmonella* Typhimurium (*S*. Tm) and as a result *Muc13*$^{-/-}$ mice are susceptible to cecal infection by *Salmonella* Typhimurium (*S*. Tm) (35). Human MUC17 is confined to small intestinal enterocytes, while murine MUC17 is expressed in both the small and large intestines. We disentangled the segment-specific function using two interventions with distinct mechanisms of action. DSS disrupts the mucus layer separating gut bacteria from the epithelium (36). Accordingly, DSS-induced colitis is rapid and severe in mouse models with mucus defects (23-25). Since glycocalyx-deficient *Muc17*$^{\Delta IEC}$ mice still produced a functional colonic mucus barrier, they were equally sensitive to colitis as wild-type controls. In an alternative intervention, we used *C. rodentium*, which shares virulence factors with enteropathogenic *Escherichia coli* (EPEC), a major human pathogen that targets the small intestine. While *C. rodentium* is typically used to study pathogen-host interactions in the mouse distal colon (37), it surprisingly colonized the jejunum, including its mucosa, in Muc17-deficient mice. This finding highlights the crucial role of MUC17 in defending the small intestine against bacterial infections, even in the presence of a functioning mucus barrier. Interestingly, the ileum of Muc17-deficient mice was more resistant to colonization by *C. rodentium* than the jejunum. This difference can be explained by the lower expression of antimicrobial peptides in the mouse jejunum compared to the ileum, making it easier for the bacteria to colonize the jejunum (38). Given the established link between ileal CD and reduced antimicrobial peptide levels (39, 40), the murine jejunum emerges as a relevant model for ileal CD in humans.

Defects in intestinal defenses frequently result in the translocation of gut bacteria to peripheral tissues (26, 29). Bacterial translocation has also recently been linked the expansion

of "creeping fat" in CD (28). Under baseline conditions, $Muc17^{\Delta IEC}$ mice exhibited an age-dependent spontaneous deterioration of epithelial homeostasis in the small intestine, involving elevated levels of host proteins participating in bacterial invasion (Arhgef26) and antimicrobial proteins such as Lyz1 and Reg3b. We attribute these host responses to increased and steadfast bacterial challenges in the absence of Muc17 and a functional glycocalyx. In line with these findings, $Muc17^{\Delta IEC}$ mice displayed greater body mass, enlargement of abdominal fat, and viable commensal bacteria in peripheral tissues, all of which further support the importance of the glycocalyx-forming MUC17 in limiting pathology related to CD.

Gel-forming mucins not only serve as a physical barrier against bacteria but also provide a habitat for bacteria that utilize mucins as a carbon source (38, 41). However, such a role for membrane mucins has not been described. Our work shows that Muc17 regulates gut microbiota composition and signifies that Muc17-dependent changes in the bacterial community propagate from the small intestine, where Muc17 exerts its function, distally towards the colon. Importantly, increased abundance of *Coriobacteriia* and *Lachnoclostridium*, enriched in $Muc17^{\Delta IEC}$ mice, has also been reported in CD patients (42-44). Thus, our study suggests that MUC17 fulfills two purposes; forming a glycocalyx that blocks bacteria and regulating the selection of bacteria by the host. We postulate that the latter function depends on the apical localization of MUC17 on microvilli, which release luminal vesicles that bind and limit bacterial growth in the lumen (16). The absence of Muc17 from microvillus-derived luminal vesicles could alter vesicle interactions with bacteria, thereby impacting the microbial community.

In conclusion, we uncovered a role for the MUC17-based glycocalyx as an important defense system of the small intestine. Our findings shed light on the regiospecific role of membrane mucins as innate defense components that create a critical interface between the host

epithelium and the gut microbiota. The disruption of this system in the non-inflamed ileum of CD patients suggests that defective MUC17 biosynthesis or trafficking is an early epithelial defect that precedes inflammation. Given the limited number of mouse models for small intestinal inflammation, the *Muc17*$^{\Delta IEC}$ model provides opportunities for understanding the molecular mechanisms underlying epithelial cell dysfunction in Crohn's disease.

Methods

Sex as a biological variable

Our study examined female and male patients. We did not observe sex-specific differences. The study also examined male and female mice, and similar findings are reported for both sexes. Thus, sex was not considered as a biological variable.

Experimental Design

We aimed to identify the molecular mechanisms by which compromised MUC17 and glycocalyx function impact disease development in ileal CD. To this end, non-inflamed ileal biopsies from CD and non-IBD patients were analyzed for MUC17 levels and glycocalyx barrier integrity. Mechanistic and functional investigations were performed using a preclinical $Muc17^{\Delta IEC}$ mouse strain, which was subjected to two distinct challenge models as well as analyzed longitudinally under baseline SFP conditions. Data collection and analysis were performed in a blinded manner whenever possible. For patient biopsies, sample size was not determined by power calculation but estimated based on our experience and previous studies. Sample sizes and statistical tests are described in the figure legends.

Human subjects

Patients (≥18 years) with Crohn's disease (CD) and individuals without suspected IBD (non-IBD), referred to Sahlgrenska University Hospital (Gothenburg, Sweden), were eligible for inclusion in the study. Clinical information and metadata for enrolled subjects are provided in Supplemental Table 1. Patients with macroscopic or microscopic evidence of intestinal pathology other than CD were excluded. Biopsies were obtained during ileocolonoscopy, using biopsy forceps routinely used in standard of care. Three biopsies were obtained from the non-inflamed terminal ileum of each subject and immediately placed into the appropriate

vials; ice-cold oxygenated Krebs transport solution (45) for *ex vivo* glycocalyx permeability

assay, 4% PFA for histology and a dry vial frozen at -80°C.

Mice

The *Muc17^{fl/fl}* mouse strain was engineered by introducing *loxP* sites flanking exons 3 and 5

of the *Muc17* gene (Ensembl gene ID: ENSMUSG00000037390; NCBI gene ID: 666339)

(Supplemental Figure 2A). To generate the *Muc17^{ΔIEC}* strain; *Muc17^{fl/fl}* were crossed with

Vil1-Cre mice (JAX Strain# 004586, RRID:IMSR_JAX:004586). All mice were on a

C57BL/6N background, maintained under standardized SPF conditions of temperature (21–

22°C), and illumination (12-hour light/dark cycle) with *ad libitum* access to food and water.

Experimental groups consisted of age- and sex-matched 6–8-week-old cohoused littermates,

or 5, 8- or 36-40-week-old mice where indicated. Animals were anesthetized with isoflurane

followed by cervical dislocation.

Ex vivo **glycocalyx permeability assay in ileal biopsies**

The barrier integrity of the glycocalyx was quantified as previously described (*9*). In detail,

biopsies from the ileum of patients were collected in ice-cold oxygenated Krebs transport

solution and pinned down with the epithelial side up in silicon-well plates. Mounted samples

were stained with 50 μg/mL CellMask Deep Red plasma membrane stain (Thermo Fisher

Scientific Cat# C10046) for 15 min. at room temperature (RT), fixed with 4% PFA for 1 hour

at RT, and washed three times with PBS. Bacterial penetration into the glycocalyx was

quantified using viable *E. coli^{GFP+}* (*9*), cultured overnight at 37°C in LB medium

supplemented with 100 μg/mL ampicillin and washed in PBS before the assay. Mounted

biopsies were incubated with *E. coli^{GFP+}* for 20 min. prior to time-lapse confocal imaging

(pixel dwell time 2.41 μsec, frame time 20.39 s) for 30 cycles using a Plan-Apochromat ×

20/1.0 DIC water-immersion objective (Zeiss), 488/639-nm lasers, on an upright LSM 700 Axio Examiner Z.1 confocal imaging system (Carl Zeiss) with Zen acquisition software (Carl Zeiss). The spatial distance of individual $E.\ coli^{GFP+}$ cells relative CellMask was extracted as a function of time using Imaris software (Oxford Instruments). The CellMask-stained brush border was reconstructed using the Isosurface function and shortest distance calculation. Individual $E.\ coli^{GFP+}$ cells were reconstructed using the Spot function and shortest distance calculation. The frequency distribution of $E.\ coli^{GFP+}$ cells in the distance interval of 0-2 µm from the CellMask-stained brush border was visualized in Prism 10 software (GraphPad). Quantification was performed on an average of 3 regions per villus and three villi per patient biopsy.

Infection of mice with *Citrobacter rodentium*

Streptomycin-resistant *C. rodentium* strain DBS100 (*44*) and chloramphenicol-resistant DBS100-derived $C.\ rodentium^{GFP+}$ (*45*) strains were used in the infection experiments. Infection inocula were cultured overnight in LB broth at 37°C in an orbital shaking incubator. Overnight cultures were concentrated 10-fold by centrifugation at 4000 RCF for 10 min. and resuspension in LB broth. Six- to eight-week-old, cohoused female and male $Muc17^{fl/fl}$ and $Muc17^{\Delta IEC}$ littermates were gavaged with 200 µL of infection inoculum (2×10^8 CFU). The end point of the experiment was as indicated in each experiment, loss of 10% of initial weight, or death. *C. rodentium* load at different tissue sites was determined by sacrificing the mice and collecting samples under aseptic conditions. Approximately 3 cm of jejunum, ileum, and distal colon were dissected and flushed with 4 mL sterile PBS to collect the contents. Contents and flushed tissue were collected separately. *C. rodentium* load was also quantified by sampling the liver, mesenteric lymph nodes, and spleen. Tissue samples were homogenized in sterile PBS using an Ultra-Turrax T10 dispersing instrument (IKA) that was

sequentially cleaned in 70% ethanol (×2) and sterile PBS. *C. rodentium* was enumerated from the homogenates by serial dilution on MacConkey agar plates supplemented with 100 µg/mL streptomycin or 30 µg/mL chloramphenicol, followed by overnight incubation at 37°C and quantification of bacterial CFUs. For each sample, a theoretical limit of detection (LOD) was calculated based on the detection of one colony at the lowest plated dilution. An average LOD is shown for each tissue sample.

Statistical Analysis

Statistical analysis and graphical illustrations were performed using Prism 10 software (GraphPad) and R open-source software. Biological replicates for each group and experiment are stated in the figure legends. All data are presented as means ± SD except the quantification CFU of *C. rodentium* (Figure 4, D-F, Supplemental Figure 5) as medians with interquartile range, quantification of total weight as median with minimum to maximum range of data points (Figure 8A), and the quantification of the 16S rRNA gene in peripheral tissues (Figure 8C), which is represented as mean ± SEM. Statistical tests were applied as indicated in each figure legend and the p-values for each statistical test are indicated in each. Principal components analysis (PCA) of genotype- and age-dependent epithelial and mucus parameters was performed using the 'princomp' function in R.

Study approval

Informed consent was obtained from all patients in accordance with the respective protocol described in the ethical permit 2020-03196 approved by the Swedish Ethical Review Authority. The Swedish Laboratory Animal Ethical Committee in Gothenburg (ethical permits 2285-19 and 2292-19) approved all experiments.

Data availability

All data are available in the main text or the supplementary material. Supporting data values

for all the described experiments are reported in Supplemental Table 4. The mass

spectrometry proteomics data have been deposited to the ProteomeXchange Consortium

(http://proteomecentral.proteomexchange.org) via the PRIDE partner repository with the

dataset identifier PXD048896.

Further information can be found in Supplemental materials.

Author contributions:

Conceptualization: ELH, TP

Methodology: ELH, SJ, LA, BD, TP

Investigation: ELH, SJ, FCvdK, MS, TP

Visualization: ELH, TP

Supervision: TP

Materials: ST, BAV, TP

Writing—original draft: ELH, TP

Writing—review & editing: ELH, SJ, FCvdK, BD, LA BAV, TP

References

1. Pelaseyed T, et al. The mucus and mucins of the goblet cells and enterocytes provide the first defense line of the gastrointestinal tract and interact with the immune system. *Immunol Rev.* 2014;260(1):8-20.
2. Gustafsson JK, and Johansson MEV. The role of goblet cells and mucus in intestinal homeostasis. *Nat Rev Gastroenterol Hepatol.* 2022;19(12):785-803.
3. Johansson MEV, et al. The inner of the two Muc2 mucin-dependent mucus layers in colon is devoid of bacteria. *Proc Natl Acad Sci U S A.* 2008;105(39):15064–9-–9.
4. van der Post S, et al. Structural weakening of the colonic mucus barrier is an early event in ulcerative colitis pathogenesis. *Gut.* 2019;68(12):2142-51.
5. Ermund A, et al. Studies of mucus in mouse stomach, small intestine, and colon. I. Gastrointestinal mucus layers have different properties depending on location as well as over the Peyer's patches. *Am J Physiol Gastrointest Liver Physiol.* 2013;305(5):G341-7.
6. Lang T, and Pelaseyed T. Discovery of a MUC3B gene reconstructs the membrane mucin gene cluster on human chromosome 7. *PLoS One.* 2022;17(10):e0275671.
7. Pelaseyed T, et al. Carbachol-induced MUC17 endocytosis is concomitant with NHE3 internalization and CFTR membrane recruitment in enterocytes. *American journal of physiology Cell physiology.* 2013;305(4):C457-67.
8. Malmberg EK, et al. The C-terminus of the transmembrane mucin MUC17 binds to the scaffold protein PDZK1 that stably localizes it to the enterocyte apical membrane in the small intestine. *Biochem J.* 2008;410(2):283-9.
9. Layunta E, et al. IL-22 promotes the formation of a MUC17 glycocalyx barrier in the postnatal small intestine during weaning. *Cell Rep.* 2021;34(7):108757.
10. Khor B, et al. Genetics and pathogenesis of inflammatory bowel disease. *Nature.* 2011;474(7351):307-17.
11. Crohn BB, et al. Regional ileitis; a pathologic and clinical entity. *Am J Med.* 1952;13(5):583-90.
12. Martin HM, et al. Enhanced Escherichia coli adherence and invasion in Crohn's disease and colon cancer. *Gastroenterology.* 2004;127(1):80-93.
13. Darfeuille-Michaud A, et al. High prevalence of adherent-invasive Escherichia coli associated with ileal mucosa in Crohn's disease. *Gastroenterology.* 2004;127(2):412-21.
14. Hampe J, et al. A genome-wide association scan of nonsynonymous SNPs identifies a susceptibility variant for Crohn disease in ATG16L1. *Nat Genet.* 2007;39(2):207-11.
15. VanDussen KL, et al. Abnormal Small Intestinal Epithelial Microvilli in Patients With Crohn's Disease. *Gastroenterology.* 2018;155(3):815-28.
16. Shifrin DA, Jr., et al. Enterocyte microvillus-derived vesicles detoxify bacterial products and regulate epithelial-microbial interactions. *Curr Biol.* 2012;22(7):627-31.
17. McConnell RE, et al. The enterocyte microvillus is a vesicle-generating organelle. *J Cell Biol.* 2009;185(7):1285-98.
18. Schneider H, et al. Study of mucin turnover in the small intestine by in vivo labeling. *Sci Rep.* 2018;8(1):5760.
19. Bhinder G, et al. The Citrobacter rodentium mouse model: studying pathogen and host contributions to infectious colitis. *J Vis Exp.* 2013(72):e50222.
20. Abrams GD, et al. Influence of the normal flora on mucosal morphology and cellular renewal in the ileum. A comparison of germ-free and conventional mice. *Lab Invest.* 1963;12:355-64.
21. Lesher S, et al. Generation Cycle in the Duodenal Crypt Cells of Germ-Free and Conventional Mice. *Nature.* 1964;202:884-6.
22. Bourgeois JS, et al. ARHGEF26 enhances Salmonella invasion and inflammation in cells and mice. *PLoS Pathog.* 2021;17(7):e1009713.
23. An G, et al. Increased susceptibility to colitis and colorectal tumors in mice lacking core 3-derived O-glycans. *J Exp Med.* 2007;204(6):1417-29.

24.   Cornick S, et al. VAMP8-mediated MUC2 mucin exocytosis from colonic goblet cells maintains innate intestinal homeostasis. *Nat Commun.* 2019;10(1):4306.
25.   Sharpen JDA, et al. Transglutaminase 3 crosslinks the secreted gel-forming mucus component Mucin-2 and stabilizes the colonic mucus layer. *Nat Commun.* 2022;13(1):45.
26.   Johansson MEV, et al. Bacteria penetrate the normally impenetrable inner colon mucus layer in both murine colitis models and patients with ulcerative colitis. *Gut.* 2013.
27.   Lkhagva E, et al. The regional diversity of gut microbiome along the GI tract of male C57BL/6 mice. *BMC Microbiol.* 2021;21(1):44.
28.   Ha CWY, et al. Translocation of Viable Gut Microbiota to Mesenteric Adipose Drives Formation of Creeping Fat in Humans. *Cell.* 2020;183(3):666-83 e17.
29.   Bergstrom JH, et al. Gram-positive bacteria are held at a distance in the colon mucus by the lectin-like protein ZG16. *Proc Natl Acad Sci U S A.* 2016;113(48):13833-8.
30.   Ma L, et al. Translocation of Lactobacillus-Murinus from the Gastrointestinal-Tract. *Curr Microbiol.* 1990;20(3):177-84.
31.   Kong L, et al. The landscape of immune dysregulation in Crohn's disease revealed through single-cell transcriptomic profiling in the ileum and colon. *Immunity.* 2023;56(2):444-58 e5.
32.   Keir M, et al. The role of IL-22 in intestinal health and disease. *J Exp Med.* 2020;217(3):e20192195.
33.   Kokkinou E, et al. The single-cell transcriptional landscape of innate and adaptive lymphocytes in pediatric-onset colitis. *Cell Rep Med.* 2023;4(5):101038.
34.   McGuckin MA, et al. Muc1 mucin limits both Helicobacter pylori colonization of the murine gastric mucosa and associated gastritis. *Gastroenterology.* 2007;133(4):1210-8.
35.   McGuckin MA, et al. MUC13 Cell Surface Mucin Limits Salmonella Typhimurium Infection by Protecting the Mucosal Epithelial Barrier. *Cell Mol Gastroenterol Hepatol.* 2023;16(6):985-1009.
36.   Johansson MEV, et al. Bacteria Penetrate the Inner Mucus Layer before Inflammation in the Dextran Sulfate Colitis Model. *PLoS ONE.* 2010;5(8):e12238-e.
37.   Nataro JP, and Kaper JB. Diarrheagenic Escherichia coli. *Clin Microbiol Rev.* 1998;11(1):142-201.
38.   Birchenough GMH, et al. Muc2-dependent microbial colonization of the jejunal mucus layer is diet sensitive and confers local resistance to enteric pathogen infection. *Cell Rep.* 2023;42(2):112084.
39.   Lamas B, et al. CARD9 impacts colitis by altering gut microbiota metabolism of tryptophan into aryl hydrocarbon receptor ligands. *Nat Med.* 2016;22(6):598-605.
40.   Wehkamp J, et al. The Paneth cell alpha-defensin deficiency of ileal Crohn's disease is linked to Wnt/Tcf-4. *J Immunol.* 2007;179(5):3109-18.
41.   Raba G, and Luis AS. Mucin utilization by gut microbiota: recent advances on characterization of key enzymes. *Essays Biochem.* 2023;67(3):345-53.
42.   Alam MT, et al. Microbial imbalance in inflammatory bowel disease patients at different taxonomic levels. *Gut Pathog.* 2020;12:1.
43.   Raygoza Garay JA, et al. Gut Microbiome Composition Is Associated With Future Onset of Crohn's Disease in Healthy First-Degree Relatives. *Gastroenterology.* 2023;165(3):670-81.
44.   Chiodini RJ, et al. Microbial Population Differentials between Mucosal and Submucosal Intestinal Tissues in Advanced Crohn's Disease of the Ileum. *PLoS One.* 2015;10(7):e0134382.
45.   Krebs HAH, K. Untersuchungen uber die Harnstoffbildung im Tierkörper. *Biological Chemistry.* 1932;210(1-2):33-66.
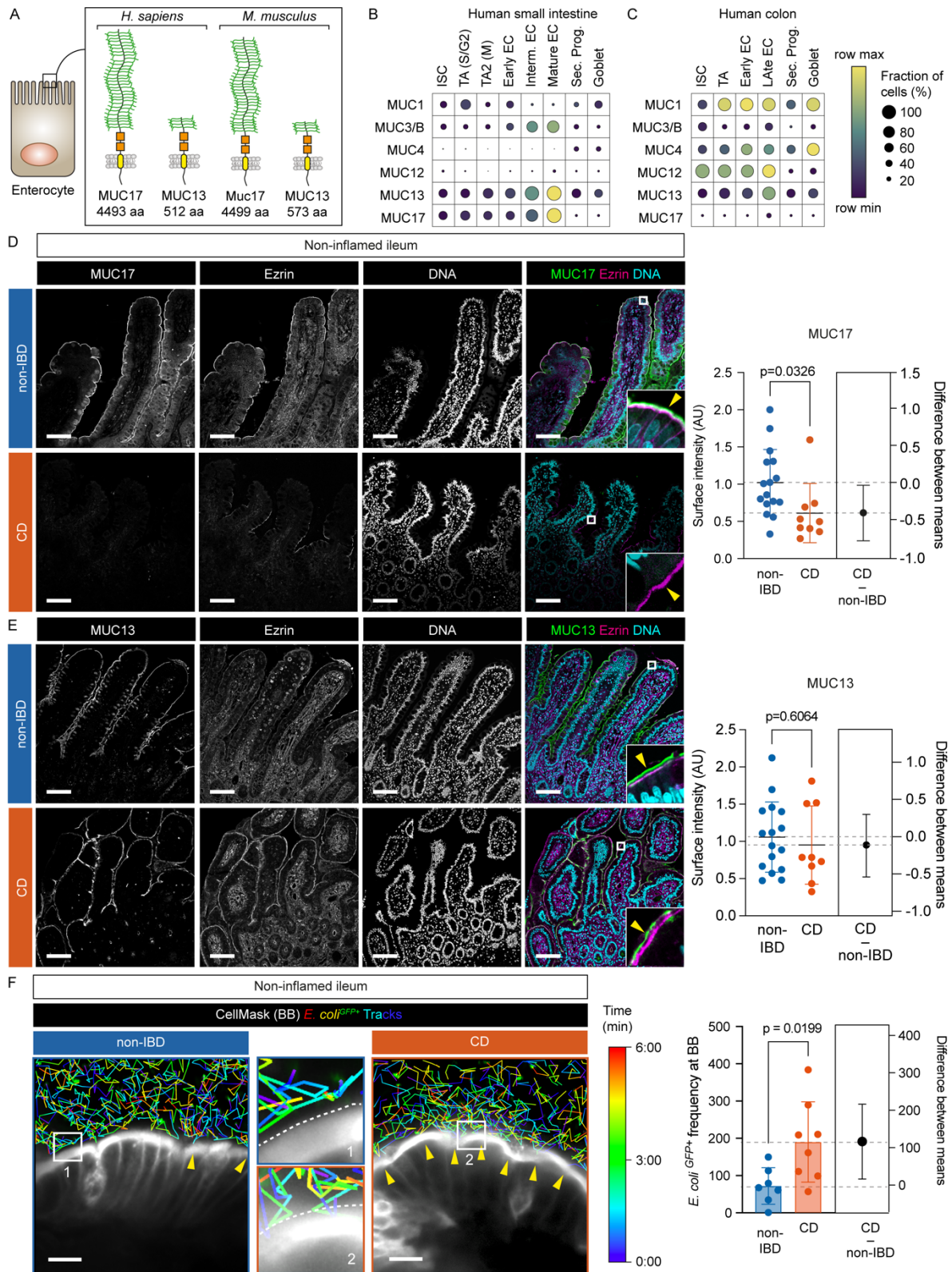
Supplementary material

Supplementary methods

Supplementary references

Supplemental Figures 1-10

Supplemental Tables 1-4

Movie 1

Figure 1. Reduced surface levels of MUC17 and a permeable glycocalyx in the non-inflamed ileum of CD patients.

(**A**) Cartoon of human and mouse MUC17 and MUC13. (**B**) Membrane mucin mRNA transcripts at single-cell resolution in human small intestinal epithelial cells. (**C**) Membrane mucin mRNA transcripts in human colonic epithelial cells. EC, enterocyte; ISC, intestinal stem cell; TA, transit amplifying; Sec. Prog., secretory progenitor; Goblet, goblet cell. S/G2, S- and G2-phase; M, M-phase. Row maximum and minimum represent relative expression of each gene among cell types. (**D**) Immunohistochemistry of MUC17 (green), Ezrin (magenta), and DNA (cyan) in sections of non-inflamed ileal biopsies from non-IBD and CD patients, alongside semiquantitative analysis of MUC17 levels in the brush border. Each channel is shown in grayscale. Yellow arrow points to the brush border. Scale bar 100 μm. n=16 for non-IBD, n=9 for CD. (**E**) Immunohistochemistry of MUC13 (green), Ezrin (magenta), and DNA (cyan) in non-inflamed ileal biopsies from non-IBD control and CD patients, alongside semiquantitative analysis of MUC13 in the brush border. Each channel is shown in grayscale. Yellow arrow points to the brush border. Scale bar 100 μm. n=16 for non-IBD, n=9 for CD. (**F**) Time-lapse glycocalyx permeability assay in non-inflamed ileal biopsies from non-IBD and CD patients, stained with CellMask and incubated with $E.\ coli^{GFP+}$ tracked over the course of 6 min. Yellow arrows show overlap between $E.\ coli^{GFP+}$ and CellMask. Dashed white line marks the brush border. Magnifications are labeled with numbers. Scale bar 10 μm. Pseudo-color scale indicates time points during tracking bacteria. Bar graph depicts frequency of $E.\ coli^{GFP+}$ attached to the brush border. n=7 for non-IBD, n= 8 for CD. Data are means ± SD. Significance was determined by unpaired t-test (D-F). Estimation plot shows the difference between CD and non-IBD means with a 95% confidence interval.
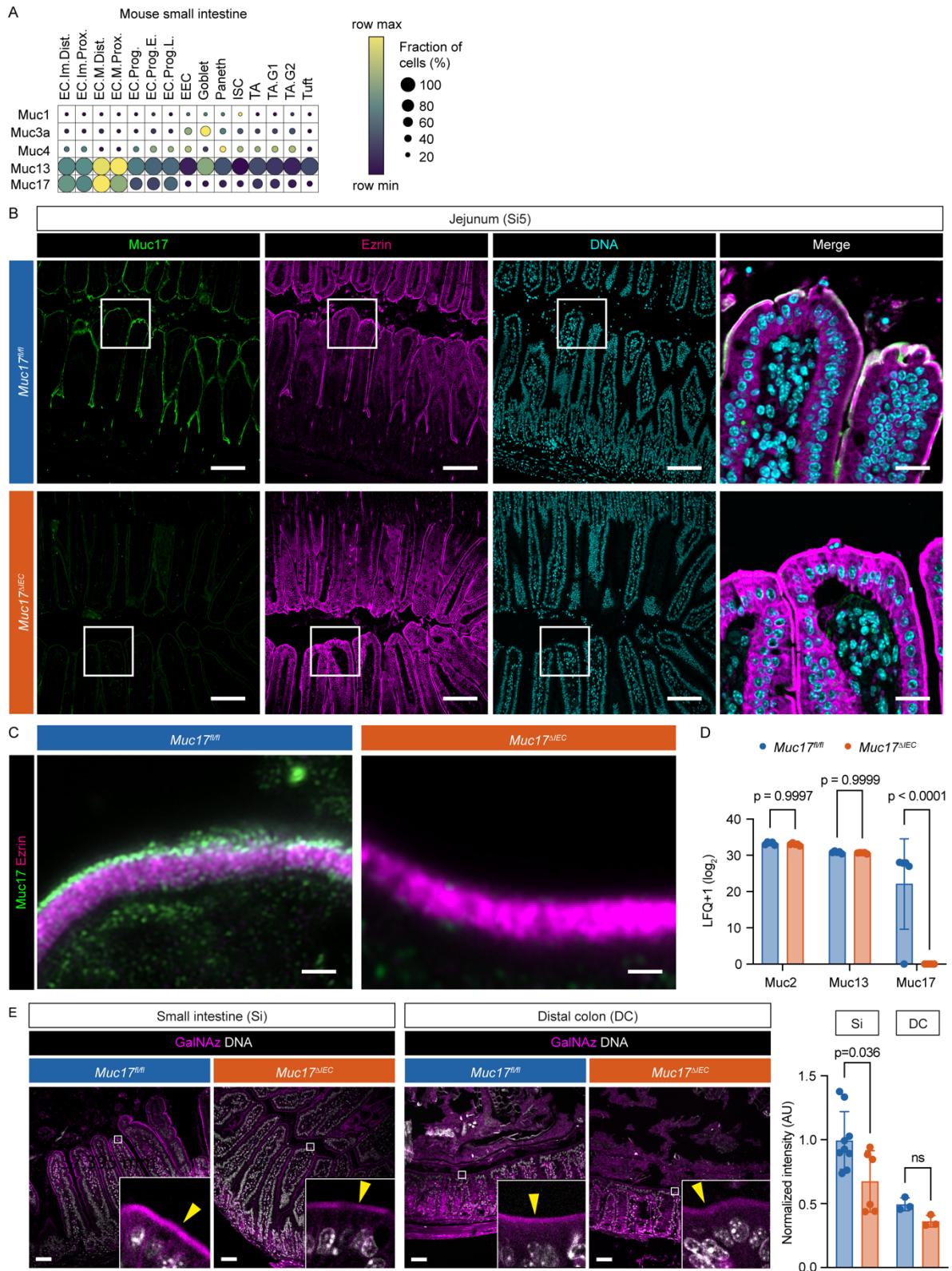
Figure 2. Epithelial-specific deletion of *Muc17* results in the loss of Muc17 expression in the mouse small intestine.

(**A**) Expression of membrane mucin transcripts in epithelial cell types of the mouse small intestine. The color scheme shows row maximum and minimum representing the relative expression of each gene among all cell types. EC, enterocyte; EEC, enteroendocrine cell; ISC, intestinal stem cell; TA, transit amplifying; Im, immature; M, mature; Prox, proximal; Dist, distal; Prog, progenitor; E, early; L, late; G1, G1-phase; G2, G2-phase of cell cycle. (**B**) Immunohistochemistry of Muc17 (green), Ezrin (magenta), and DNA (cyan) in histological sections of the jejunum (Si5) from *Muc17$^{fl/fl}$* and *Muc17$^{\Delta IEC}$* mice. Scale bar 50 µm. Scale bar in insets 10 µm. (**C**) Airyscan high-resolution microscopy of Muc17 (green) and Ezrin (magenta) in the small intestinal brush border of *Muc17$^{fl/fl}$* and *Muc17$^{\Delta IEC}$* mice. Scale bar 1 µm. (**D**) Bar graph representing the abundance of detected mucins in the proteome of small intestinal epithelial cells from *Muc17$^{fl/fl}$* and *Muc17$^{\Delta IEC}$* mice. n= 5 for each group. (**E**) Representative confocal micrographs of small intestine (Si) and distal colon (DC) from *Muc17$^{fl/fl}$* and *Muc17$^{\Delta IEC}$* mice, stained for bioorthogonally labeled *O*-glycans (GalNAz, magenta) and DNA (white). Scale bar 50 µm. Bar graphs represent the quantification of GalNAz intensity in the apical brush border of the small intestine (Si) and DC in each group. Si5: n=6-9 per group. DC: n=3 per group. Significance was determined by two-way ANOVA followed by Šidák correction (D) and Mann-Whitney test (E).
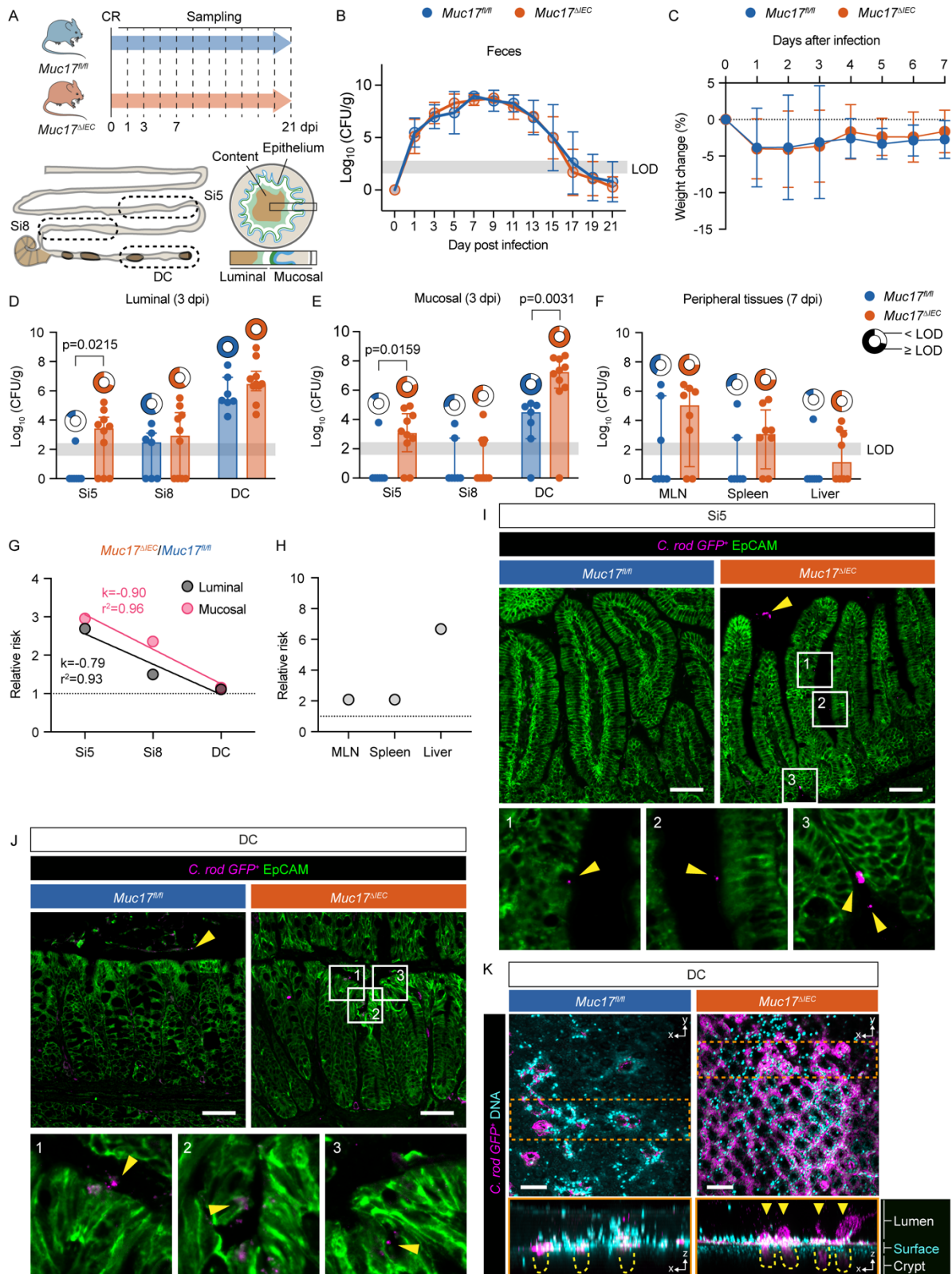
Figure 3. Deletion of Muc17 results in abnormal small intestinal susceptibility to *C. rodentium* infection.

(**A**) Infection protocol and sampling time points. Si5, jejunum; Si8, ileum; DC, distal colon. (**B**) *C. rodentium* colony forming units (CFU) in fecal samples at various days post-infection (dpi). (**C**) Weight loss of infected *Muc17$^{fl/fl}$* and *Muc17$^{\Delta IEC}$* mice as percent of the initial weight at 0 dpi. (**D**) *C. rodentium* CFU in luminal compartments of Si5, Si8, and DC at 3 dpi. (**E**) *C. rodentium* CFU in mucosal compartments of Si5, Si8, and DC at 3 dpi. (**F**) *C. rodentium* CFU in mesenteric lymph nodes (MLN), Spleen, and Liver at 7 dpi. Circle charts represent proportion of mice with CFU above the limit of detection (LOD) in each segment or tissue site. (**G**) Relative risk of carrying *C. rodentium* CFU above LOD in Si5, Si8, and DC luminal and mucosal compartments. n=6-10 per group. (**H**) Relative risk of carrying *C. rodentium* CFU above LOD in MLN, Spleen, and liver. n=6-10 per group. (**I**) Immunohistochemistry of *C. rodentium^{GFP+}* (magenta) in relation to epithelium (EpCAM, green) in Si5 of *Muc17$^{fl/fl}$* and *Muc17$^{\Delta IEC}$* mice 3 days post-infection. Yellow arrows point to bacterial cells. Scale bar 50 μm. (**J**) Immunohistochemistry of *C. rodentium^{GFP+}* (magenta) in relation to epithelium (EpCAM, green) in DC of *Muc17$^{fl/fl}$* and *Muc17$^{\Delta IEC}$* mice 3 days post-infection. Yellow arrows point to bacterial cells. Scale bar 50 μm. (**K**) Visualization of *C. rodentium^{GFP+}* (magenta) in relation to epithelium (DNA, cyan) in explants of *Muc17$^{fl/fl}$* and *Muc17$^{\Delta IEC}$* DC 3 days post-infection. Upper panels show top view (xy plane) and lower panels show extended orthogonal view (xz plane) of boxed region (orange). Penetration of *C. rodentium^{GFP+}* (magenta) into colonic crypts (yellow dashed lines) is highlighted (yellow arrows). Scale bar 100 μm. Significance was determined by Mann-Whitney test (D-F).
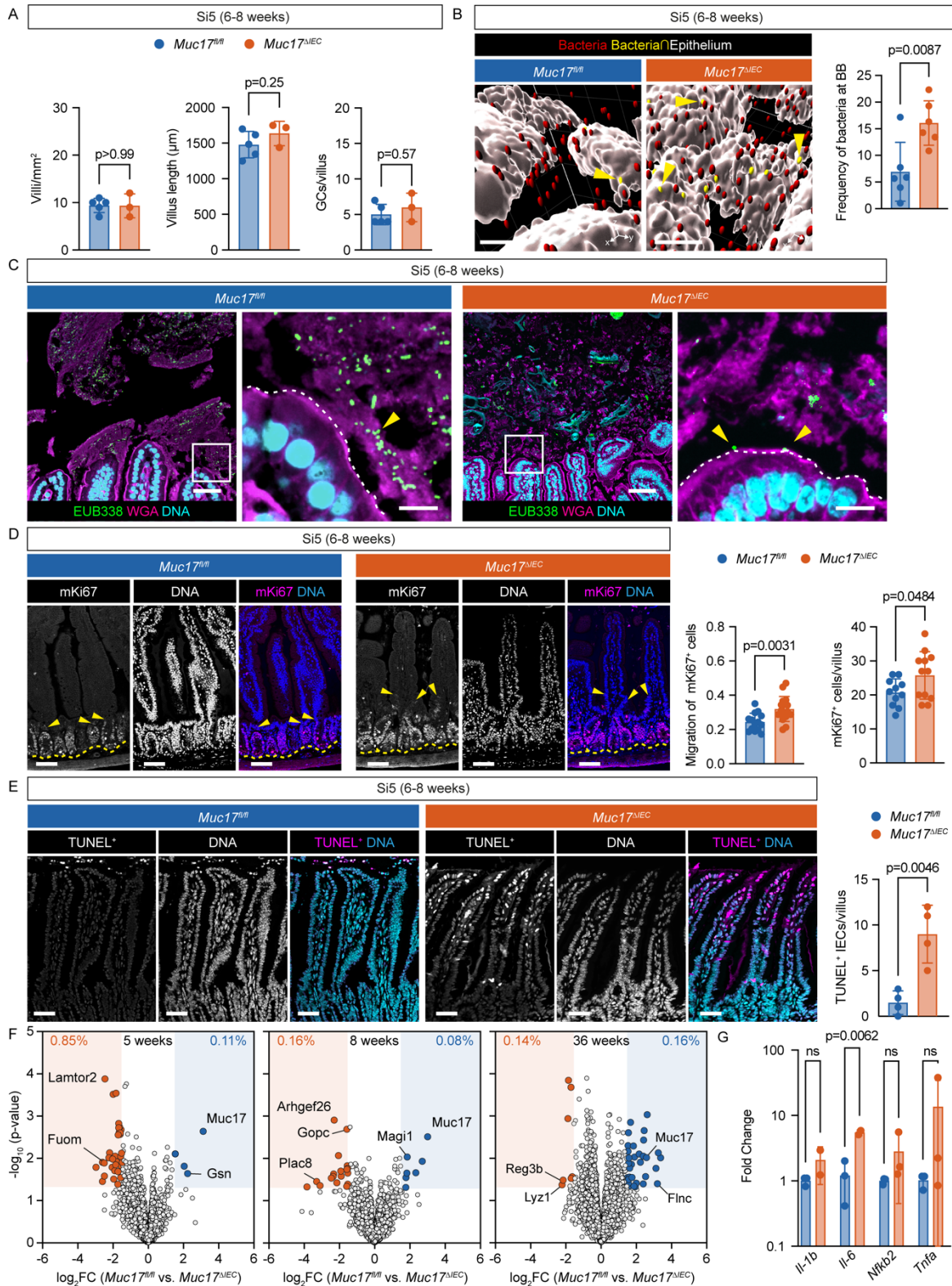
Figure 4. Epithelial barrier dysfunction in *Muc17^{ΔIEC}* small intestine under SFP conditions.

(**A**) Quantification of villi per mm^2 of histological section, villus length, and goblet cells (GCs) per villus in *Muc17$^{fl/fl}$* and *Muc17$^{\Delta IEC}$* jejunum (Si5). n=5 for *Muc17$^{fl/fl}$*, n=3 for *Muc17$^{\Delta IEC}$*. (**B**) Visualization of commensal bacteria (red) on Si5 epithelium (white). Bacteria in contact with epithelium are shown in yellow. Scale bar 100 μm. Quantification shows frequency of bacteria attached to the brush border in each cohort. n=6 for *Muc17$^{fl/fl}$*, n=6 for *Muc17$^{\Delta IEC}$*. (**C**) *Muc17$^{fl/fl}$* and *Muc17$^{\Delta IEC}$* Si5 stained for bacteria (EUB338, green), epithelium and mucus (WGA, magenta), and DNA (cyan). Yellow arrows point to bacteria. Scale bar 25 μm. Scale bar in insets 10 μm. (**D**) Immunohistochemistry of mKi67 (magenta) and DNA (blue) in *Muc17$^{fl/fl}$* and *Muc17$^{\Delta IEC}$* Si5. Each channel is shown in grayscale. Yellow arrows point to mKi67$^+$ cells with maximum migration along villus-crypt axis. Yellow line depicts the crypt bottom. Scale bar 50 μm. Quantification of mKi67$^+$ cell migration along crypt-villus axis and absolute numbers of mKi67$^+$ per villus in *Muc17$^{fl/fl}$* and *Muc17$^{\Delta IEC}$* Si5. n=3-6 villi per mouse, 3 mice per group. (**E**) Immunohistochemistry of TUNEL$^+$ nuclei (magenta) and DNA (cyan) in *Muc17$^{fl/fl}$* and *Muc17$^{\Delta IEC}$* Si5. Each channel is shown in grayscale. Scale bar 50 μm. Quantification of TUNEL$^+$ cells per villus in *Muc17$^{fl/fl}$* and *Muc17$^{\Delta IEC}$* mice. n=4 for *Muc17$^{fl/fl}$*, n=4 for *Muc17$^{\Delta IEC}$*. (**F**) Volcano plots showing protein abundance in epithelial cells of Si5 from 5-, 8-, and 36-week-old *Muc17$^{fl/fl}$* compared to *Muc17$^{\Delta IEC}$* mice. Differentially expressed proteins (fold change ≥ 2, p-value < 0.05) are highlighted with filled circles. n=5 for each genotype in each age group. (**G**) Expression of *Il-1b, Il-6, Nfkb2, and Tnfa* genes in Si5 of *Muc17$^{fl/fl}$* and *Muc17$^{\Delta IEC}$* mice. Significance was determined by Mann-Whitney test (A) and unpaired t-test (B, D, E, G).

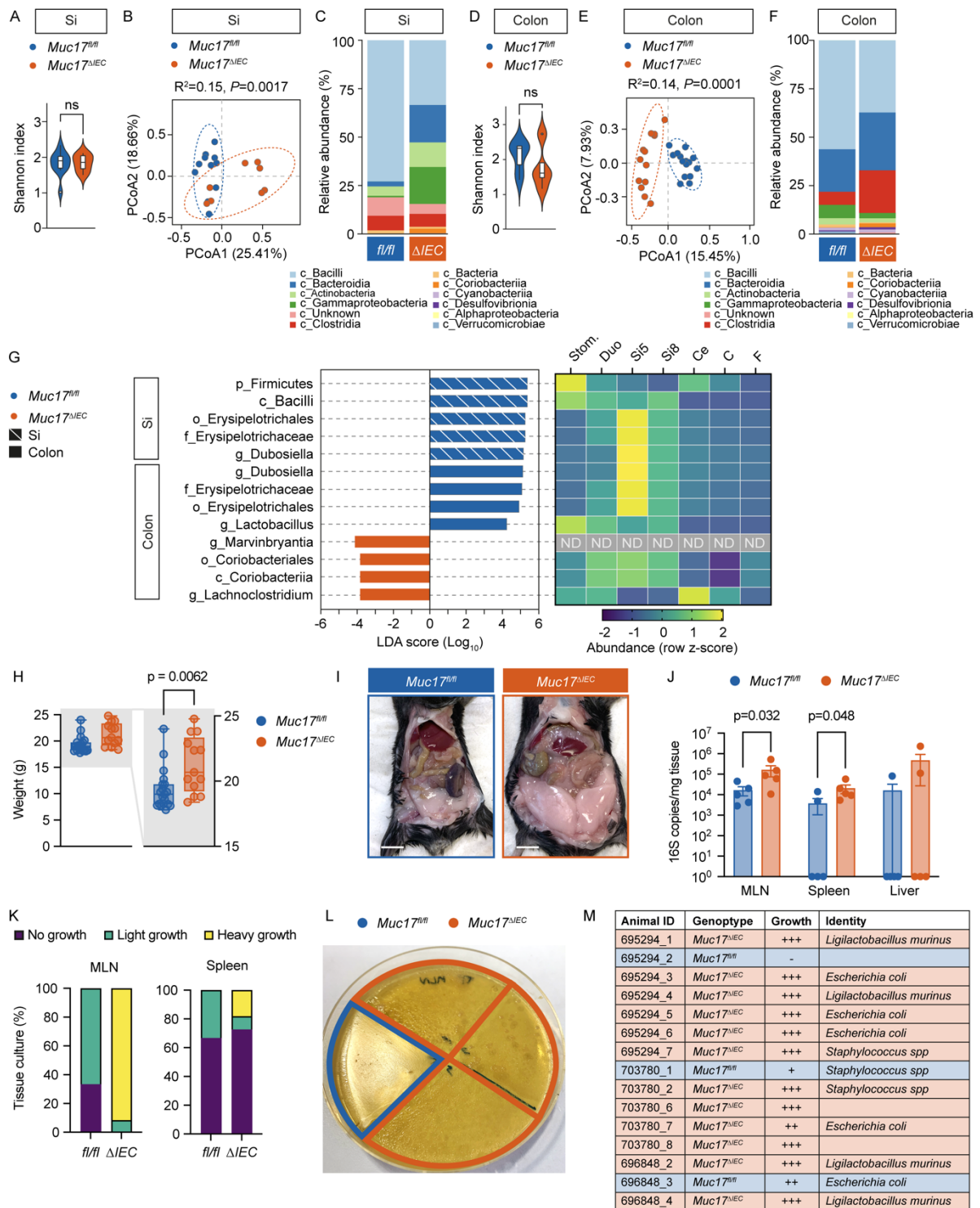**Figure 5. Deletion of Muc17 results in alterations in luminal microbiota composition and translocation of commensal bacteria to peripheral tissues.**

(**A**) α-diversity (Shannon index) of luminal bacterial communities in the small intestine (Si) of *Muc17*^*fl/fl*^ (n=11) and *Muc17*^*ΔIEC*^ (n=8) mice. (**B**) Principal coordinate analysis of β-

diversity (Bray-Curtis dissimilarity) of luminal bacterial communities of $Muc17^{fl/fl}$ and $Muc17^{\Delta IEC}$ Si. (**C**) Relative frequency of major classes found in $Muc17^{fl/fl}$ and $Muc17^{\Delta IEC}$ Si. (**D**) α-diversity (Shannon index) of luminal bacterial communities in the colon of $Muc17^{fl/fl}$ (n=15) and $Muc17^{\Delta IEC}$ (n=13) mice. (**E**) Principal coordinate analysis of β-diversity (Bray-Curtis dissimilarity) of luminal bacterial communities in $Muc17^{fl/fl}$ and $Muc17^{\Delta IEC}$ colon. (**F**) Relative frequency of major classes found in $Muc17^{fl/fl}$ and $Muc17^{\Delta IEC}$ colon. (**G**) Linear discriminant analysis (LDA) effect size identification of small intestinal and colonic taxa that differentiate between $Muc17^{fl/fl}$ (blue) and $Muc17^{\Delta IEC}$ (red) mice. The heat map shows the row z-score representing the relative abundance of the selected taxa in different gastrointestinal segments. Stom, stomach; Duo, duodenum; Si5, jejunum; Si8, ileum; Ce, cecum; C, colon; F, feces; ND, not detected. (**H**) Total weight of cohoused $Muc17^{fl/fl}$ (n=19) and $Muc17^{\Delta IEC}$ (n=13) littermate mice. Box plots show the median and minimum to maximum values for each group. (**I**) Representative image of the opened abdomen of 36-40-week-old $Muc17^{fl/fl}$ and $Muc17^{\Delta IEC}$ mice. Scale bar 1 cm. (**J**) Quantification of bacterial 16S copy number in mesenteric lymph nodes (MLN), spleen, and Liver tissue by qPCR. n= 5 for each group. (**K**) Quantification of bacterial growth in tissue homogenates of MLN and spleen on BHIS agar plates under anaerobic conditions. (**L**) Representative image representing bacterial growth in tissue homogenates of MLN on BHIS agar under anaerobic conditions. (**M**) Identification of isolated bacterial colonies identified by 16S rDNA sequencing. Significance was determined by unpaired t-test (A) and Mann-Whitney test (C).